Creep trajectory transition of a nonstationary viscoelastic model onto a single rate parameter

H. Tanaka[1,*] G. Yamanokuchi,[1] and Y. Shibutani[1,2]

[1]*Department of Mechanical Engineering, Osaka University, 2-1 Yamadaoka, Suita, Osaka 565-0871, Japan*

[2]*Nanotechnology Program, VNU Vietnam Japan University, Luu Huu Phuoc Street, My Dinh 1 Ward, Nam Tu Liem District, Ha Noi, Viet Nam*

A system of three-variable differential equations, which has a nonstationary trajectory transition through the control of a single rate parameter, is formulated. For the nondimensional system, the critical trajectory creeps before a transition in a long-lasting plateau region in which the velocity vector of the system hardly changes and then diverges positively or negatively in finite time. The mathematical model well represents the compressive viscoelasticity of a spring-damper structure simulated by the multibody dynamics analysis. In the simulation, the post-transition behaviors realize a tangent stiffness of the self-contacted structure that is polarized after transition. The mathematical model is reduced not only to concisely express the abnormal compression problem, but also to elucidate the intrinsic mechanism of creep-to-transition trajectories in a general system.

I. INTRODUCTION

A system of nonlinear differential equations concisely describes complicated physical phenomena with drastic transitions, such as bifurcations. Typical bifurcating behaviors can be categorized as pitchfork bifurcations, transcritical bifurcations, saddle-node bifurcations, and Hopf bifurcations [1], which are represented by a simple velocity form of ordinary differential equations (ODEs) with control parameters.

The control parameters are the criteria of bifurcation; with changes in the parameters, fixed points emerge, coalesce, and collide and annihilate to reform the system stability. As an example, a one-dimensional supercritical pitchfork bifurcation is expressed by $dx/dt = \partial U(x; \lambda)/\partial x = \lambda x - x^3$, where U is the potential function and $(x, \lambda) \in \mathbb{R}^2$. Here, the origin ($x = 0$) is stable when $\lambda < 0$, but is destabilized when $\lambda > 0$, instead of there being two stable fixed points ($x = \pm\sqrt{\lambda}$) [2,3]. Thus, by increasing λ, the new fixed points emerge and the nature of the original fixed point is altered.

One pitchfork bifurcation system applied in physics is the buckling of static and dynamic structures, such as multiple-linked rods and beam-column members [4–7]. Column buckling under the critical compression load, referred to as *Euler load* [4], is a well known engineering problem concerning structural instability and is a class of supercritical pitchfork bifurcations. Another type of buckling, snap-through buckling, occurs in a bistable state and is an example of imperfect pitchfork bifurcation; an additional control parameter is used for the imperfection [8–10]. Similar to analogous unstable phenomena, the collective buckling behaviors of microstructures such as honeycombs have been studied extensively [11–17], and the active harnessing of buckling morphology of microstructures has been proposed recently [18–20].

In contrast, a one-dimensional transcritical bifurcation is expressed by $dx/dt = \lambda x - x^2$. The system has the two fixed points of $x = 0$ and $x = \lambda$ for $\lambda \in \mathbb{R}\backslash 0$. A stability assessment around the fixed points shows that the origin is stable and the point at $x = \lambda$ is unstable when $\lambda > 0$, and vice versa when $\lambda < 0$. Thus, by increasing λ, the fixed points coalesce as $\lambda = 0$ and then reemerge such that their stability changes. If λ and t are replaced with K and rt/K in the differential equation, the equation reduces to the logistic growth model [21]: $dx/dt = rx(1 - x/K)$, where r and K are positive constants in general. This conversion is an example in which the bifurcation mechanism mathematically has physical and ecological applications, and the transcritical bifurcation really appears in a control system of the logistic model [22].

As stated in our brief review of the two bifurcation groups above, nonlinear systems have a variety of transition mechanisms and allow us to investigate actual phenomena with multiple degrees of freedom, as in the example of mode changes of an axial compression to deflection in continuum column buckling. In this study, we present another concept of transition behavior by developing the three-variable differential equations of a nonequilibrium system without fixed points. In our previous study, we proposed a compressive transformability of a two-dimensional microstructure made up of square linkages based on switching the coordinate square rotation [23–25]. Modeling the microstructure under a periodic framework with two degrees of freedom revealed that the transition behavior is characterized by changes in the hyperplane of a hyperbolic paraboloid when increasing the internal spring constant [26].

Here we extend the static elastic model to the viscoelastic model subjected to a uniaxial compression with a constant loading rate. We thus derive a system of ODEs with three variables and a control rate parameter. By analyzing the initial value problem, we show that the critical trajectory of time-dependent variables slowly traces a moving saddle point and bifurcates in the positive or negative direction
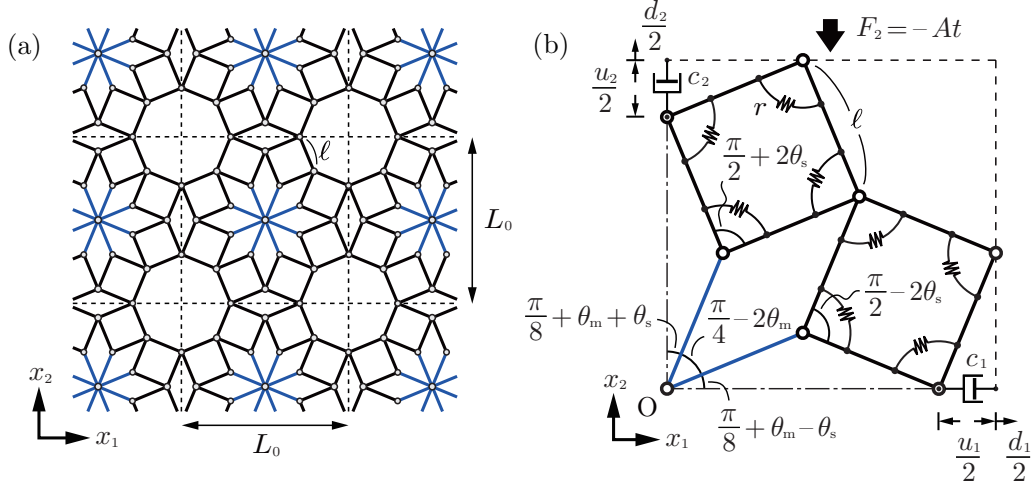
*htanaka@mech.eng.osaka-u.ac.jp

FIG. 1. (a) Proposed periodic bar-joint framework and (b) the unit cell with the first of four structural elements. The structure is linked by rotational springs and linear dampers. The two angular variables, θ_m and θ_s, determine the transformation of the framework.

of divergence within a finite time. For this application, we conduct the multibody dynamics (MBD) simulation of the two-dimensional self-contacted microstructure and conclude that different compression load rates polarize the tangent stiffness after transformation.

II. MODEL EQUATIONS

Figure 1(a) presents a periodic framework made from two types of rigid bar, pivotally connected through hinged joints in a square-lattice fashion; a blue straight bar has twice the length of a black bar [26], where the length of the identical black bar is denoted ℓ and the cell length is denoted L_0 at the undeformed state. Excluding shear motion, the mechanical structure has two degrees of freedom, represented by the internal angular variables θ_m and θ_s [see Fig. 1(b)]. The structure transforms into a square pattern with $\theta_m = -\pi/8$ and $\theta_s = 0$ and a diamond pattern with $\theta_m = \pi/8$ and $\theta_s = 0$. The structure has stiffness determined by the rotational springs and two types of linear damper. The former components reinforce the inside square linkages with a rotational spring coefficient k_θ and the latter components are inserted horizontally and vertically between adjacent cells with damping coefficients c_1 and c_2, respectively [Fig. 1(b)].

We now consider the proposed structure subjected to the vertical force F_2 in the x_2-axial direction. We assume the proportional compressive loading as $F_2 = -At$ at time t for a compression rate of A. We let t^* be the nondimensional time, expressed as $t^* = t/T_0$ with a time constant T_0. We introduce two dimensionless compression variables,

$$A^* = \frac{A\ell T_0}{16k_\theta}, \quad c_i^* = \frac{c_i \ell^2}{16k_\theta T_0}, \quad \text{for } i \in \{1, 2\}. \quad (1)$$

For convenience, the angular variables θ_m and θ_s are converted into three variables:

$$\begin{aligned}
\xi(t^*) &= q[\theta_m(t^*) + \theta_s(t^*)] - p, \\
\eta(t^*) &= -q[\theta_m(t^*) - \theta_s(t^*)] + p, \\
\zeta(t^*) &= A^* t^*,
\end{aligned} \quad (2)$$

where $p = \cos(\pi/8)$, $q = \sin(\pi/8)$ and the initial position is denoted $(\xi_0, \eta_0, \zeta_0) \equiv [\xi(0), \eta(0), \zeta(0)] = (-p, p, 0)$. Reducing the compression problem to its weak nonlinear form, we obtain nondimensional ODEs with the three variables ξ, η, and ζ,

$$\begin{aligned}
(\xi + \eta) - 2(p\xi + 1)\zeta + c_1^* p^2 \dot{\xi} &= 0, \\
(\xi + \eta) - q\eta\zeta + c_2^* p^2 \dot{\eta} &= 0, \\
\dot{\zeta} &= A^*,
\end{aligned} \quad (3)$$

where the overdot symbol indicates a time derivative; i.e., $\dot{\mathcal{X}} \equiv d\mathcal{X}/dt^*$. The detailed derivation of Eq. (3) is described in Appendix A. In Eq. (3), the acceleration terms are ignored under the assumption of slow viscoelastic behavior.

III. ANALYSES OF THE VELOCITY SYSTEM

The velocity form of Eq. (3) is expressed with the control rate parameter A^* as

$$\begin{aligned}
\dot{\xi} &= \frac{1}{c_1^* p^2}[-(\xi + \eta) + 2\zeta(p\xi + 1)], \\
\dot{\eta} &= \frac{1}{c_2^* p^2}[-(\xi + \eta) + q\zeta\eta], \\
\dot{\zeta} &= A^*.
\end{aligned} \quad (4)$$

According to the initial-value problem of Eq. (4) with (ξ_0, η_0, ζ_0), which corresponds to $\theta_m = \theta_s = 0$ as $t = 0$ [see Eq. (A15)], the nondimensional system obviously has the nonstationary behavior that ζ increases proportionally with an increase in t^*.

Let $\boldsymbol{x}(t^*) = [\xi(t^*), \eta(t^*), \zeta(t^*)]^\mathsf{T}$ be the position vector. Equation (4) is rewritten as $\dot{\boldsymbol{x}} = \boldsymbol{F}(\boldsymbol{x}(t^*); A^*)$ in a vector fashion. The time-integrated trajectory is then obtained from $\boldsymbol{x}(t^*) = \boldsymbol{x}_0 + \int_0^{t^*} \boldsymbol{F}(\boldsymbol{x}(\tau); A^*)d\tau$, where $\boldsymbol{x}_0 = (-p, p, 0)^\mathsf{T}$. Using the high-order Runge-Kutta method, we computed $\boldsymbol{x}(t^*)$ with increasing A^*. For $c_1^* = c_2^* = 1$, Figs. 2(a)–2(c) show three diagrams of the trajectories projected onto the (ξ, η) plane, (ξ, ζ) plane, and (η, ζ) plane for $A^* \in [0.002, 0.07]$ at intervals of $\Delta A^* = 2 \times 10^{-3}$. The time domain is $t^* \in [0, 14]$
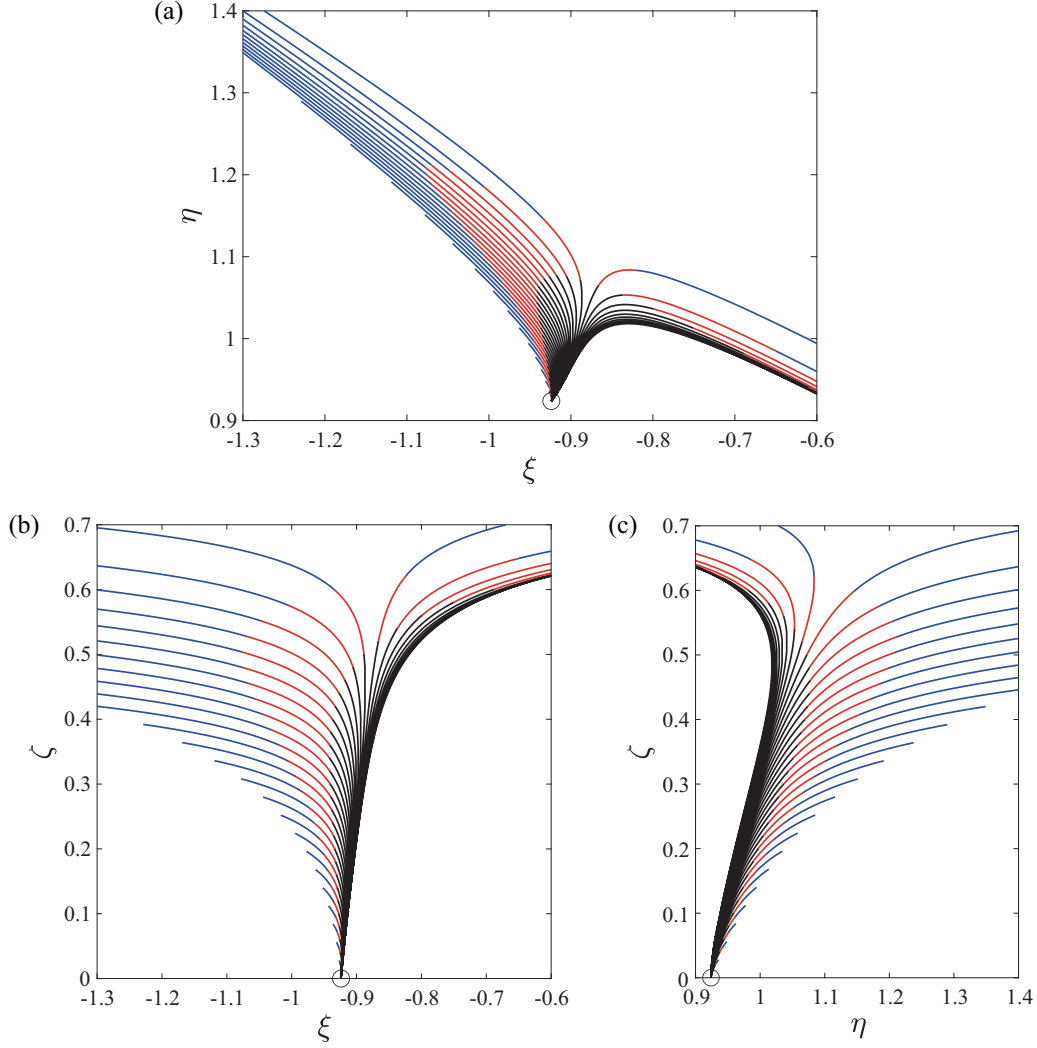
FIG. 2. Trajectories of Eq. (4) with $c_1^* = c_2^* = 1$ from $(-p, p, 0)$ within $A^* \in [0.002, 0.07]$: (a) (ξ, η) plane, (b) (ξ, ζ) plane, and (c) (η, ζ) plane. The interval of A^* is 2×10^{-3}. The paths are truncated at $t^* = 10$ (black), $t^* = 12$ (red), and $t^* = 14$ (blue). The center of each circle indicates the initial position.

in each diagram and the black, red, and blue paths, respectively, correspond to truncations at $t^* = 10$, 12, and 14. For the slow motions at small values of A^*, the ξ values tend to decrease after increasing a little from the initial position, indicated by a circle, while the η values increase monotonically [see Fig. 2(a)]. With increasing A^*, the trajectory behavior changes at the critical value of A^*; thus, the ξ values increase monotonically and the η values decrease after increasing to some extent. In the temporal progression of ξ and η in the ζ direction [Figs. 2(b) and 2(c)], shifts in the trajectory behaviors are confirmed in the vicinity of the critical A^*.

To understand the trajectory transition, we investigate the velocity field of Eq. (4) at each level of a fixed ζ, i.e., on the hyperplane (ξ, η). At a constant $\zeta = \zeta_c$, the system has a single stationary point that satisfies $\dot{\xi} = \dot{\eta} = 0$, except at the initial position where $\zeta_c = 0$. The stationary point (ξ', η') is expressed as

$$\xi' = -\frac{2(q\zeta_c - 1)}{2pq\zeta_c - (2p + q)}, \quad \eta' = -\frac{2}{2pq\zeta_c - (2p + q)}. \quad (5)$$

Removing ζ_c from Eq. (5) and replacing ξ' and η' with ξ and η, we have

$$\eta = \frac{2}{q}(p\xi + 1). \quad (6)$$

Equation (6) gives the moving line of (ξ', η') for a parameter ζ_c. The first-order Taylor expansion of Eq. (4) at the point (ξ', η') yields

$$\begin{pmatrix} \dot{\xi} \\ \dot{\eta} \end{pmatrix} = \begin{pmatrix} \dfrac{2p\zeta_c - 1}{c_1^* p^2} & -\dfrac{1}{c_1^* p^2} \\ -\dfrac{1}{c_2^* p^2} & \dfrac{q\zeta_c - 1}{c_2^* p^2} \end{pmatrix} \begin{pmatrix} \xi - \xi' \\ \eta - \eta' \end{pmatrix}. \quad (7)$$

We obtain the eigenvalues of the Jacobian matrix in Eq. (7) as $\lambda_1 = (a + b)/2$ and $\lambda_2 = (a - b)/2$, where a and b are written as

$$a = \frac{2p\zeta_c - 1}{c_1^* p^2} + \frac{q\zeta_c - 1}{c_2^* p^2},$$

$$b = \left[\left(\frac{2p\zeta_c - 1}{c_1^* p^2} - \frac{q\zeta_c - 1}{c_2^* p^2} \right)^2 + \frac{4}{c_1^* c_2^* p^4} \right]^{1/2}. \quad (8)$$
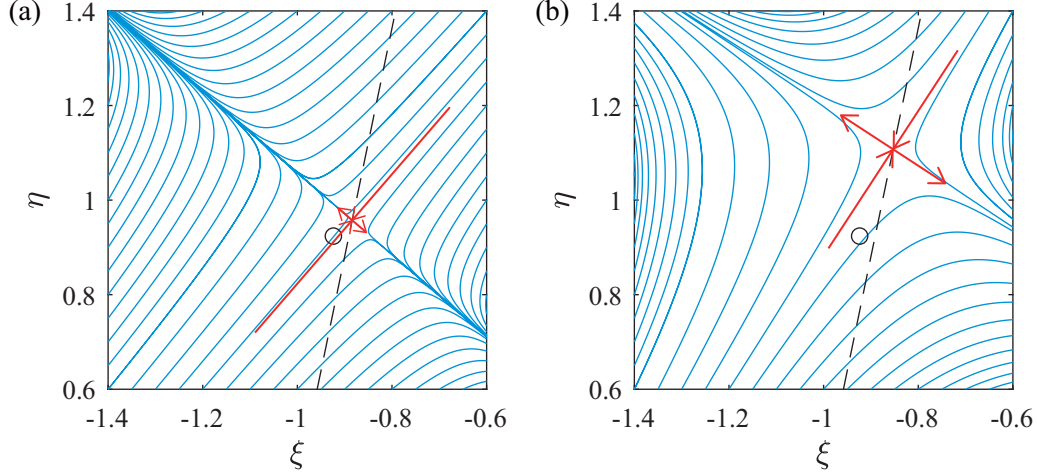
FIG. 3. Phase portraits (streamline-wise plots) of Eq. (4) on the (ξ, η) planes of (a) $\zeta_c = 0.2$ and (b) $\zeta_c = 0.6$, where $c_1^* = c_2^* = 1$. The red arrows indicate the eigenvectors multiplied by their eigenvalues at the stationary point, i.e., $s\lambda_i \boldsymbol{n}_i$ ($s = 0.15$). The dashed line indicates a set of stationary points expressed by Eq. (6). The center of a circle indicates the initial position.

When $\zeta < (2p + q)/(2pq) \approx 3.1543$, $\lambda_1 > 0$ and $\lambda_2 < 0$ because $a^2 < b^2$ and $b > 0$. Hence, the finite stationary point of Eq. (5) has a saddle instability. The normalized eigenvectors corresponding to $\lambda_{i \in \{1,2\}}$ are

$$\boldsymbol{n}_i = \frac{\boldsymbol{y}_i}{|\boldsymbol{y}_i|}, \quad \boldsymbol{y}_i = \begin{pmatrix} \pm(q\zeta_c - 2 - c_2^* p^2 \lambda_i) \\ \mp(2p\zeta_c - 2 - c_1^* p^2 \lambda_i) \end{pmatrix}, \quad (9)$$

where $i \in \{1, 2\}$.

Figures 3(a) and 3(b) present streamline-wise plots in the velocity field of Eq. (4) at $\zeta_c = 0.2$ and 0.6, respectively, where the red arrows located at (ξ', η') are displayed with the corresponding eigenvectors of Eq. (9) to $\lambda_{i \in \{1,2\}}$. To compare Figs. 3(a) and 3(b), the stationary point (ξ', η') is elevated with increasing ζ_c, which changes the streamlines around the circle indicating the initial position, i.e., the streamline positioned at (ξ_0, η_0, ζ_c) shifts in the negative (positive) direction of ξ when ζ_c is small (large). Therefore, when A^* is high, the trajectory can achieve a high level of ζ_c without being affected by the flow field at the low level, which results in the transition seen in Figs. 2(b) and 2(c).

IV. CHARACTERIZATION OF THE VISCOELASTIC MODEL

We analyze the specific case of our proposed spring-damper structure to characterize whether a trajectory transition occurs and what the transition behavior is. We conclude in advance that the model with $c_1^* = 0$ has a trajectory transition, whereas there is no transition when $c_2^* = 0$. We then discuss the mechanism that depends on the critical rate parameter to formulate the polar coordinate system for $c_1^* = 0$.

A. Case of $c_1^* = 0$

Considering only vertical damping (i.e., $c_1^* = 0$), the first equation of (3) becomes

$$(\xi + \eta) - 2(p\xi + 1)\zeta = 0 \quad \text{for } \forall A^*$$

$$\Leftrightarrow -(2p\zeta - 1)(p\xi + 1) + (p\eta - 1) = 0 \quad \text{for } \forall A^*. \quad (10)$$

Equation (10) imposes on the system a constrained linear relation of ξ and η for an arbitrary A^* at a fixed ζ. The lines inevitably pass through the same point $(\xi_1, \eta_1) \equiv (-1/p, 1/p)$. We now consider the narrow-angle domain Ω_1 on the projected (ξ, η) plane sided by $\eta = -\xi$ and $\eta = \eta_1$, corresponding to $\zeta = 0$ and $\zeta = 1/2p$ in Eq. (10); thus,

$$\Omega_1 = \{(\xi, \eta) \in \mathbb{R}^2 \mid \xi + \eta > 0, \ \eta < \eta_1\}. \quad (11)$$

In the domain Ω_1, which includes the initial position $(\xi_0, \eta_0) = (-p, p)$, the system runs within the finite time $t^* \in [0, 1/(2pA^*))$.

Substituting the relation of Eq. (10) into the second equation of Eq. (4), we obtain equations without ζ and ξ:

$$\dot{\eta} = \frac{(\xi + \eta)[-2(p\xi + 1) + q\eta]}{2c_2^* p^2 (p\xi + 1)} \quad (12)$$

$$\text{or} \quad \dot{\eta} = \frac{\zeta[(2pq\zeta - 2p - q)\eta + 2]}{c_2^* p^2 (2p\zeta - 1)}. \quad (13)$$

Equation (13) shows that the system has a blow-up of solutions at the finite time of $t^* \uparrow 1/2pA^*$, where $\uparrow$ indicates that t^* approaches from the left. The first derivative of ξ with respect to t^* is obtained from Eq. (10) as

$$\frac{d}{dt^*}\left(\frac{p\eta - 1}{p\xi + 1}\right)$$
$$= 2\dot{\zeta} \Leftrightarrow (p\eta - 1)\dot{\xi} - (p\xi + 1)\dot{\eta} = -2(p\xi + 1)^2 A^*$$
$$\Leftrightarrow \dot{\xi} = \frac{1}{2p\zeta - 1}[\dot{\eta} - 2(p\xi + 1)A^*]. \quad (14)$$

Equations (13) and (14) yield $(\dot{\xi}(0), \dot{\eta}(0)) = (2q^2 A^*, 0)$ at the initial position of (ξ_0, η_0). In contrast, when $\xi \to \xi_1$, $\eta \to \eta_1$ for $\zeta < 1/2p$,

$$\dot{\eta} \to \frac{pq\zeta}{c_2^*}, \quad \dot{\xi} \to \frac{\dot{\eta}}{2p\zeta - 1} = \frac{pq\zeta}{c_2^*(2p\zeta - 1)}. \quad (15)$$

Equations (13) and (14) also yield the ξ-directional divergence of the system: $\lim_{\zeta \uparrow 1/2p} \dot{\xi} = \infty$ if $\dot{\eta} < 0$ and $\xi > \xi_1$, and $\lim_{\zeta \uparrow 1/2p} \dot{\xi} = -\infty$ if $\dot{\eta} > 0$ and $\xi \leqslant \xi_1$.
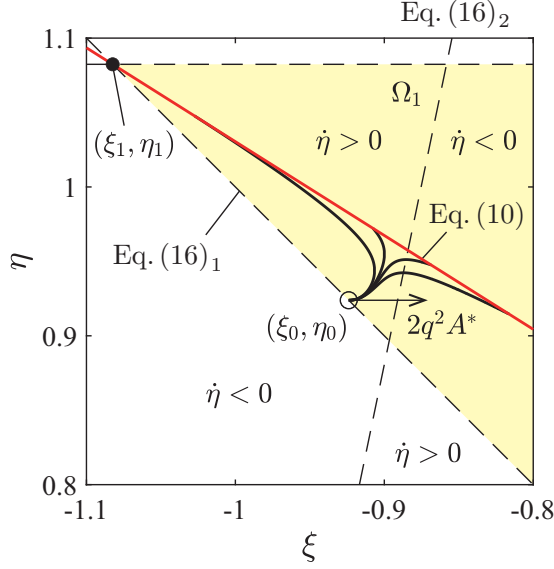
FIG. 4. Viscoelastic behaviors of Eqs. (13) and (14) with $c_2^* = 1$. The normal and solid circles, respectively, indicate (ξ_0, η_0) and (ξ_1, η_1). The yellow area corresponds to Ω_1. The red line indicates Eq. (10) for $\zeta = 0.2$; the four trajectories of $A^* \in \{0.015, 0.016, 0.0165, 0.0175\}$ are numerically integrated up to $\zeta = 0.2$ in common. The rightward arrow indicates the initial velocity.

From Eq. (12), we have two conditions of $\dot{\eta} = 0$:

$$\xi + \eta = 0 \quad \text{and} \quad -2(p\xi + 1) + q\eta = 0. \quad (16)$$

Equations (16) determine the sign of $\dot{\eta}$. By solving $\dot{\eta} = 0$ as a function of ζ in Eq. (13) with $\zeta \neq 0$, we have $\eta = -2/(2pq\zeta - 2p - q) \equiv \eta'$ as in Eq. (5). Substituting $\eta = \eta'$ into Eq. (10) gives $\xi = \xi'$, which does not correspond to the stationary state of Eq. (5) because $\dot{\xi} \neq 0$ as in Eq. (14) with $\dot{\eta} = 0$. From Eq. (14), the velocity condition of $\dot{\xi} = 0$ is $\dot{\eta} = 2(p\xi + 1)A^* > 0$ in Ω_1.

Figure 4 illustrates the viscoelastic behaviors of the system with $c_1^* = 0$ and $c_2^* = 1$, where the yellow area corresponds to the domain Ω_1. All of the trajectories begin with the rightward velocity of $2q^2 A^*$. A set of the temporal positions for all A^* is represented by the linear equation (10) as shown in Fig. 4 by the red line at $\zeta = 0.2$. It is satisfied that $\dot{\eta} = 0$ on the two dashed lines in Eqs. (16), and there are two types of trajectories in Ω_1; one type turns leftward with $\dot{\eta} > 0$ and eventually passes through (ξ_1, η_1) and the other type turns rightward, crossing the dashed line of the second equation of Eq. (16). Hence, there is a critical value between $A^* = 0.016$ and 0.0165 that yields the trajectory transition.

B. Case of $c_2^* = 0$

In Eq. (3), the system with only horizontal dampers ($c_2^* = 0$) for an arbitrary A^* obeys

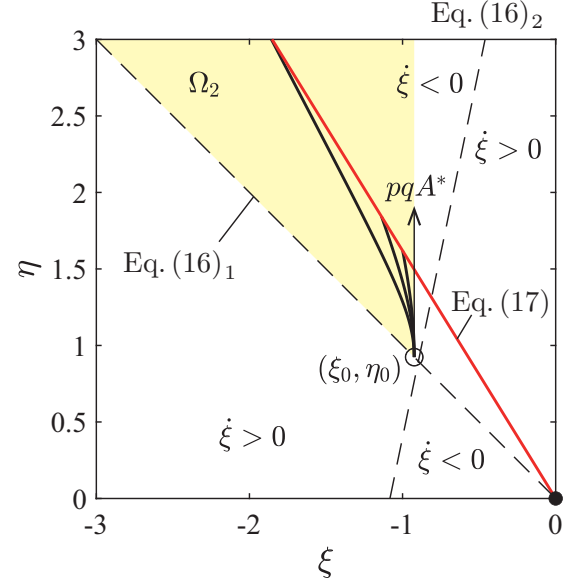$$\frac{\xi}{\eta} = q\zeta - 1 \Leftrightarrow \eta = \frac{1}{q\zeta - 1}\xi, \quad (17)$$

FIG. 5. Viscoelastic behaviors of Eqs. (19) and (20) with $c_1^* = 1$. Open and solid circles, respectively, indicate (ξ_0, η_0) and $(0,0)$. The yellow area corresponds to Ω_2. The red line indicates Eq. (17) at $\zeta = 1$. The three trajectories of $A^* \in \{0.5, 1, 2\}$ are numerically integrated up to $\zeta = 1$ in common. The upward arrow indicates the initial velocity.

and

$$\dot{\xi} = -\frac{(\xi + \eta)[-2(p\xi + 1) + q\eta]}{c_1^* p^2 q\eta} \quad (18)$$

$$\text{or} \quad \dot{\xi} = \frac{\zeta}{c_1^* p^2}\left[\frac{(2pq\zeta - 2p - q)\xi}{(q\zeta - 1)} + 2\right]. \quad (19)$$

Equation (17) indicates the linearity between ξ and η at a fixed ζ, passing through the origin. The slope of Eq. (17) ranges from -1 to infinity in the region of $\zeta \in [0, 1/q)$. The first derivative of both sides of Eq. (17) with respect to t^* gives

$$\frac{d}{dt^*}\left(\frac{\xi}{\eta}\right) = qA^* \Leftrightarrow \dot{\eta} = \frac{\eta}{\xi}(\dot{\xi} - q\eta A^*). \quad (20)$$

Equations (19) and (20) yield $\dot{\xi}(0) = 0$ and $\dot{\eta}(0) = pqA^*$ at the initial position. The conditions of $\dot{\xi} = 0$ in Eq. (18) are consistent with Eq. (16) and it is satisfied that $\dot{\xi} < 0$ where $\eta > -\xi$ and $q\eta > 2(p\xi + 1)$.

Figure 5 illustrates the viscoelastic behaviors of the system with $c_1^* = 1$ and $c_2^* = 0$, where the yellow area corresponds to the domain Ω_2, expressed by

$$\Omega_2 = \{(\xi, \eta) \in \mathbb{R}^2 \mid \xi + \eta > 0, \ \xi < \xi_0\}. \quad (21)$$

The red line shows that Eq. (17) governs the trajectory behaviors within Ω_2. Because $(\dot{\xi}, \dot{\eta}) = (0, pqA^*)$ at $\zeta = 0$ and $\dot{\xi} < 0$ in Ω_2, the trajectories for all A^* are driven leftward such that no bifurcating trajectory exists anywhere.

C. Polar coordinate system for $c_1^* = 0$

In Sec. IV A, we mentioned the transition scenario of Eq. (3) with $c_1^* = 0$. We described the system behavior under
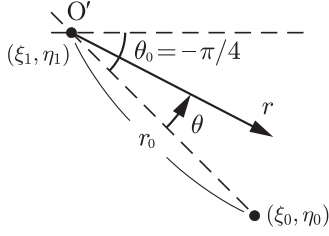
FIG. 6. Schematic of the polar coordinated system.

the constrained equation (10) of (ξ, η, ζ) such that ξ and η are variables that are dependent on each other. Here we introduce a polar coordinate system for $c_1^* = 0$ to reduce the three dependent variables to two independent variables, which enables us to assess with high accuracy the critical value of A^* for the shift in trajectory.

Figure 6 is a schematic of the polar coordinate system with (r, θ), where the initial position (r_0, θ_0) and the origin O′ correspond to (ξ_0, η_0) and (ξ_1, η_1) in the system of orthogonal coordinates (ξ, η). The polar conversion is described by

$$r = \sqrt{(\xi - \xi_0)^2 + (\eta - \eta_0)^2}, \quad \tan \theta = 2p\zeta - 1, \quad (22)$$

where $(r_0, \theta_0) = (\sqrt{2}q^2/p, -\pi/4)$ and $\theta \in [-\pi/4, 0)$ corresponding to $\zeta \in [0, 1/2p)$. Using Eq. (22), $\dot{\eta}$ of Eq. (12) and $\dot{\zeta} = A^*$ are, respectively, expressed as

$$\dot{r} = \frac{1}{\sin \theta} \left[\frac{\tan \theta + 1}{c_2^* p^2} \left(r_0 - r \cos \theta + \frac{q}{2p} r \sin \theta \right) \right.$$
$$\left. - 2pr A^* \cos^3 \theta \right],$$
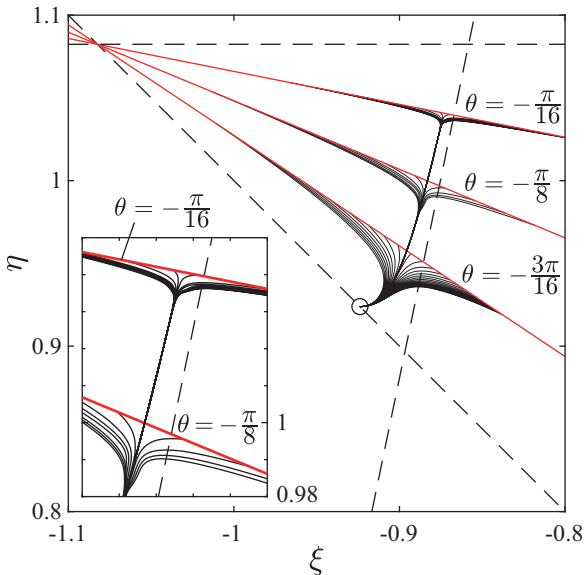$$\dot{\theta} = 2p A^* \cos^2 \theta. \quad (23)$$

FIG. 7. Trajectories computed using Eq. (23) with $c_2^* = 1$; three rate increments $\Delta A^* = 2.5 \times 10^{-4}$, 2.5×10^{-8}, and 2.5×10^{-17} are used for $\theta = -3\pi/16$, $-\pi/8$, and $-\pi/16$.

Figure 7 shows the numerical time integration of Eq. (23) with $c_2^* = 1$ obtained using the MATLAB ODE solver [27]. We performed the calculation for three scales of the rate increment: $\Delta A^* = 2.5 \times 10^{-4}$, 2.5×10^{-8}, and 2.5×10^{-17}. The minimum order is close to the limitation of the software with 16-significant-digit precision by default. These calculations give the critical value

$$A^* \approx 0.016\,164\,160\,369\,603\,70 \equiv A_{cr}^*. \quad (24)$$

With an increase in θ, the range of the load rates that enable the trajectories to attain the level of θ is reduced exponentially. As an example, rising from $\theta = -\pi/8$ to $-\pi/16$, the allowable range around $A^* = A_{cr}^*$ reduces from $\sim 10^{-7}$ to $\sim 10^{-16}$ (see the inset of Fig. 7).

The positions, velocities, and accelerations of the moving radius, i.e., $r(t^*)$, $\dot{r}(t^*)$, and $\ddot{r}(t^*)$, are calculated for the four load rates of $A^* \in \{0.01, A_{cr}^* \mp \delta, 0.02\}$, as shown in Figs. 8(a) and 8(b), where $c_2^* = 1$ and δ is the infinitesimal number of 1×10^{-17}. In the critical behaviors when $A^* = A_{cr}^* \mp \delta$, there are long-lasting plateaus, and the values of the velocity and acceleration are sufficiently low (in particular, $\ddot{r}$ is almost zero) to compare with the value for the position around 0.22. Let ϵ be an infinitesimal parameter as defined in Appendix A; the second equation of Eq. (23) gives $\dot{\theta} \sim A^* \in O(\epsilon^2)$ and $\ddot{\theta} \sim (A^*)^2 \in O(\epsilon^4)$, which are higher than the order of $\dot{r}$ and $\ddot{r}$, respectively. Therefore, both the radial and circumferential accelerations, $a_r = \ddot{r} - r\dot{\theta}^2$ and $a_\theta = r\ddot{\theta} + 2\dot{r}\dot{\theta}$, can be ignored and each order of the three types of motion variable in the time series matches the presumptions of Eqs. (A10)–(A12) for leading the system equation (3). In other words, in the vicinity of A_{cr}^*, there is creep before transition, but rapid progress in the positive or negative direction after transition.

V. DYNAMIC SIMULATION FOR A SELF-CONTACT STRUCTURE

To compare with the analyses of the viscoelastic model only with vertical dampers described in Sec. IV, we perform the MBD simulation of a unit cell including the inertial terms of the members without trigonometric approximations. We next extend the MBD simulation by taking member-to-member contact into account and investigate the tangent stiffness of the viscoelastic model after post-transition behaviors.

Physically, the momentum inertia and the self-contact of the internal members are not ignored in general. To resolve such a complicated problem, we employed MBD software (Adams [28]). The details of the modeling of MBD are described in Appendix B. Setting $c_2^* = 1$, we obtain a time constant and proportional compressive load from Eq. (1) as

$$T_0 = \frac{c_2 \ell^2}{16 k_\theta}, \quad F_2 = -\frac{16 k_\theta A^* t}{\ell T_0}. \quad (25)$$

The physical parameters used in this simulation are listed in Table I.

Figure 9 compares the (θ_m, θ_s) curves calculated using the viscoelastic model in Eq. (23) and those obtained from MBD simulation. In the MBD simulation, the trajectory
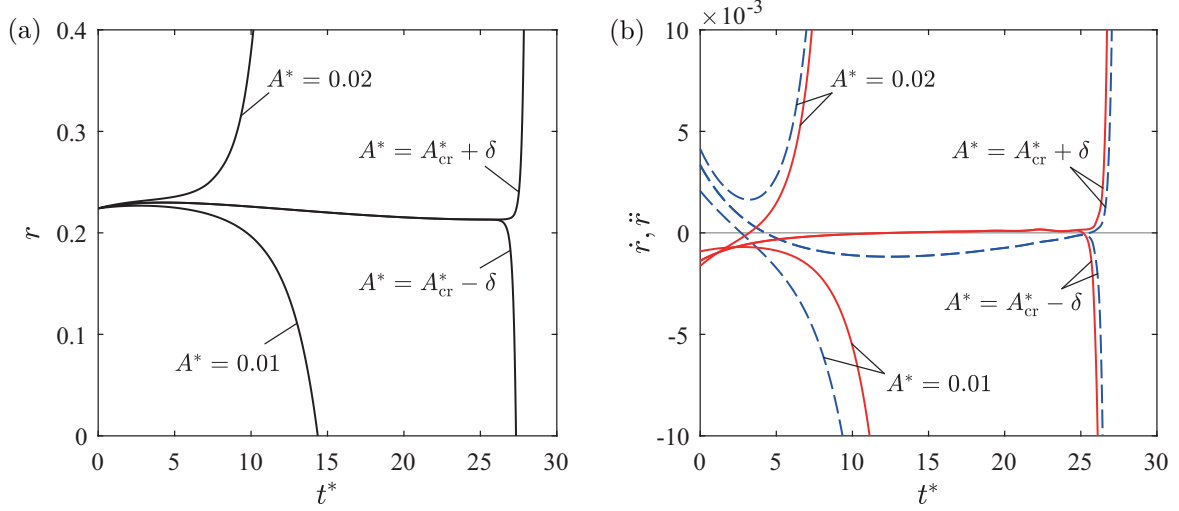
FIG. 8. Time responses of the moving radius with $c_2^* = 1$ for $A^* \in \{0.01, A_{cr}^* \mp \delta, 0.02\}$: (a) r vs t^*; (b) $\dot{r}$ vs t^* (blue dashed curves) and $\ddot{r}$ vs t^* (red solid curves). A_{cr}^* is the critical value given by Eq. (24) and $\delta = 1 \times 10^{-17}$.

transition arises in the range $A^* \in \{0.0159, 0.0160\}$, which agrees with the results of the viscoelastic model for $A^* \in \{0.0161, 0.0162\}$. Therefore, the formulation of modeling with approximations in Appendix A is adequate. The transformed structure approaches a squarelike pattern as $A^* = 0.0159$ or a diamondlike pattern as $A^* = 0.0160$ (see the insets of Fig. 9 and the Supplemental Material movies S1 and S2 [29]).

If we consider member-to-member contact inside the structure, which is possible on the dashed lines in Fig. 9, the overall tangent stiffness is altered drastically because of the strong anisotropy of square cells; i.e., axially loaded squares have high rigidity relative to the rigidity of diamonds [24,25]. We let ε_2^* denote the effective axial strain of a unit cell in the x_2 direction as expressed by $\varepsilon_2^* = d_2/L_0$ (with the tensile strain being positive), where $L_0 = 2\ell(2p + q)$ is the length of the unit cell in the initial configuration [Fig. 1(a)]. Figure 10 shows the relationship between the nondimensional force and displacement ($|F_2^*|$ vs $|\varepsilon_2^*|$) for several values of A^*. As $A^* \leqslant 0.015$, the tangent stiffness rises at $|\varepsilon_2^*| \approx 0.1$, whereas there is no rapid increase beyond $A^* = 0.016$. Note that the complete squares of $(\theta_m, \theta_s) = (-\pi/8, 0)$ correspond to $\varepsilon_2^* = 2/(2p + q) - 1 \approx -0.1033$, calculated using Eq. (A3). The viscoelastic response of switching rigidity is induced by the

geometry of the transformed microstructure as seen in the insets of Fig. 9.

VI. CONCLUSIONS

We clarified that the nondimensional system of differential equations with three variables represents a shifting trajectory through the control of a rate parameter. At the critical value
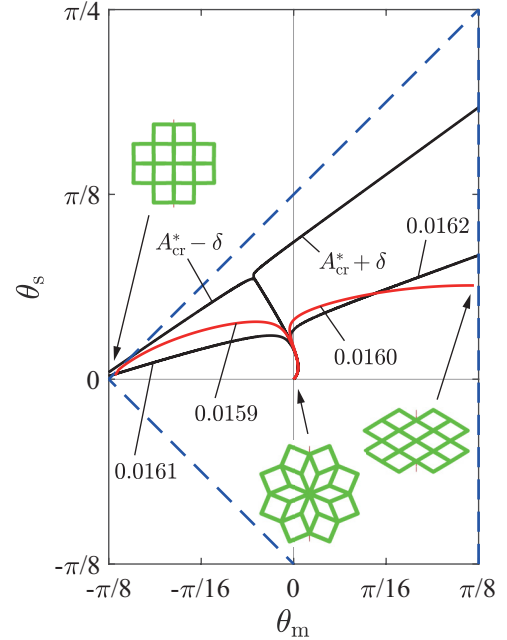

FIG. 9. Comparison of the (θ_m, θ_s) curves for the viscoelastic model and MBD analyses, where $A^* \in \{0.0161, A_{cr}^* \mp \delta, 0.0162\}$ in the model and $A^* \in \{0.0159, 0.0160\}$ in the MBD. The dashed blue curves indicate the contact boundary of $\pi/8 + \theta_m \pm \theta_s = 0$ and $\theta_m = \pi/8$ as in Fig. 1. The structure shapes in the inset are obtained by the visualization of the MBD results.

TABLE I. Geometric and material parameters.

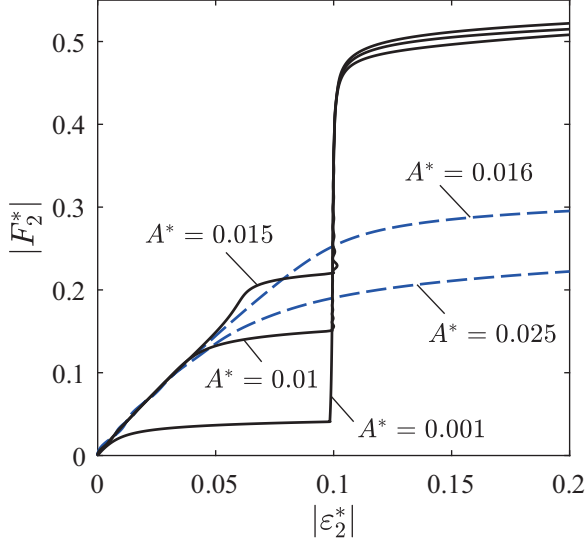|		
Beam link	length (ℓ)	200 mm
	width	40 mm
	depth	20 mm
	density	7.801×10^{-7} kg/mm^3
Spherical joint	radius	1 mm
	density	4.380×10^{-7} kg/mm^3
Rotational spring	coefficient (k_θ)	10 N mm/deg
Damper	coefficient (c_2)	1.0 N s/mm
Repulsive force	coefficient (α)	10^{-10} N mm^{13}

FIG. 10. $|F_2^*|$ vs $|\varepsilon_2^*|$ in the self-contact MBD simulation. The black solid curves indicate the post-transition transformations toward a squarelike pattern for $A^* \in \{0.001, 0.01, 0.015\}$; the blue dashed curves indicate the post-transition transformations toward a diamondlike pattern for $A^* \in \{0.016, 0.025\}$.

of the parameter, the system behavior proceeds at a slow pace and then diverges instantaneously after transition.

We first developed a nondimensional time evolution equation with ξ, η, and ζ by considering the compression problem of the spring-damper structure with two degrees of freedom. Using the velocity form of the viscoelastic model, we analyzed the initial-value problem and showed that the trajectory is shifted at the critical value of the rate parameter A^*. We then linearized the system around a saddle point. The streamlines around the nonstationary point in the (ξ, η) hyperplane are altered at each level of $\zeta = A^* t^*$, which results in the transition responses to A^*.

The specific cases of the system with $c_1^* = 0$ or $c_2^* = 0$ determine whether the system has a transition; thus, they are reduced to two-variable differential equations including a constraint condition. The trajectory diagram shows that the former case requires a trajectory shift beyond a rate threshold, whereas the latter case does not. The polar coordinate conversion of the former system into (r, θ) enables us to understand the detailed behavior of the critical trajectory for $A^* = A_{\mathrm{cr}}^*$. The time responses of r, $\dot{r}$, and $\ddot{r}$ make it clear that there is a long-lasting plateau of a moving radius r before r shifts to the positive or negative divergence in the finite time t^*. This phenomenon verified the neglect of the inertial term and the use of trigonometric approximations in formulating the system equation.

Last, we presented MBD analyses of the spring-damper structure, which gave transition behaviors similar to those of the simple viscoelastic model. The self-contact implementation provided an interesting relationship between the nondimensional force and displacement, showing polarized tangent stiffness (being rigid in a slow response or soft in a quick response; i.e., bistiffness of converse viscoelasticity). The bistiffness property is attributed to the anisotropic feature

of the bifurcating geometry toward a squarelike or diamondlike pattern.

Using the mathematical model reduced with proper approximations, we succeeded in describing the abnormal compression behaviors of the microstructure that potentially has bistiffness dependent on the loading rate. The system of ODEs with three variables exhibits a different bifurcation assembled with creep-to-transition trajectories, which is not classified into the existing bifurcation groups. For the sake of simplicity, the nonlinear equation modeling could be applied to unknown bifurcating phenomena in multidisciplinary fields.

APPENDIX A: DERIVATION OF THE NONSTATIONARY VISCOELASTIC MODEL

Here we derive the ODEs in Eq. (3) from the spring-damper structure illustrated in Fig. 1. For convenience, the two angular variables are converted to

$$\phi = \theta_{\mathrm{m}} + \theta_{\mathrm{s}}, \quad \psi = \theta_{\mathrm{m}} - \theta_{\mathrm{s}}. \tag{A1}$$

The horizontal and vertical displacements of a unit cell are then

$$
\begin{aligned}
d_1 = 2\ell \bigg[& 2\cos\left(\frac{\pi}{8} + \psi\right) + \sin\left(\frac{\pi}{8} + \phi\right) \\
& - 2\cos\frac{\pi}{8} - \sin\frac{\pi}{8} \bigg],
\end{aligned} \tag{A2}
$$

$$
\begin{aligned}
d_2 = 2\ell \bigg[& 2\cos\left(\frac{\pi}{8} + \phi\right) + \sin\left(\frac{\pi}{8} + \psi\right) \\
& - 2\cos\frac{\pi}{8} - \sin\frac{\pi}{8} \bigg],
\end{aligned} \tag{A3}
$$

and the elongations of the horizontal and vertical dampers are

$$u_1 = \ell \left[\sin\left(\frac{\pi}{8} + \phi\right) - \sin\frac{\pi}{8} \right], \tag{A4}$$

$$u_2 = \ell \left[\sin\left(\frac{\pi}{8} + \psi\right) - \sin\frac{\pi}{8} \right]. \tag{A5}$$

The time derivatives of Eqs. (A4) and (A5) are expressed as

$$\dot{u}_1 = \ell \left[\dot{\phi} \cos\left(\frac{\pi}{8} + \phi\right) \right], \quad \dot{u}_2 = \ell \left[\dot{\psi} \cos\left(\frac{\pi}{8} + \psi\right) \right], \tag{A6}$$

where we now set $\dot{\phi} = d\phi/dt$ and $\dot{\psi} = d\psi/dt$. Under the energy consideration per unit cell subjected to the x_2-directional force F_2 ($= -At$), the potential and dispersion function, denoted U and D, are expressed as

$$U = 32 \cdot \frac{1}{2} k_\theta (2\theta_{\mathrm{s}})^2 + F_2 d_2, \quad D = 2\left(\frac{1}{2} c_1 \dot{u}_1^2 + \frac{1}{2} c_2 \dot{u}_2^2\right). \tag{A7}$$

The kinetic energy per unit cell is expressed as

$$K = \tfrac{1}{2}I_\phi \dot{\phi}^2 + \tfrac{1}{2}I_\psi \dot{\psi}^2, \tag{A8}$$

where I_ϕ and I_ψ are the moments of inertia with respect to ϕ and ψ.

Let L be the Lagrangian for the system, i.e., $L = K - U$. The motion equations of the unit cell are

$$\frac{d}{dt}\left(\frac{\partial L}{\partial \dot{\phi}}\right) - \frac{\partial L}{\partial \phi} + \frac{\partial D}{\partial \dot{\phi}} = 0,$$

$$\frac{d}{dt}\left(\frac{\partial L}{\partial \dot{\psi}}\right) - \frac{\partial L}{\partial \psi} + \frac{\partial D}{\partial \dot{\psi}} = 0. \tag{A9}$$

To reduce the order of the motion equations (A9), we assume that the two angular variables belong to $\phi \in O(\epsilon)$ and $\psi \in O(\epsilon)$, where O is Landau's symbol, meaning "of the order of," and ϵ is an infinitesimal parameter. We also assume that the critical behavior of our interest proceeds slowly on the basis of viscosity, and we define it by

$$t^* = \frac{t}{T_0} \in O(\epsilon^{-1}), \quad A^* = \frac{A\ell T_0}{16 k_\theta} \in O(\epsilon^2),$$

$$c_{i \in \{1,2\}}^* = \frac{c_{i \in \{1,2\}} \ell^2}{16 k_\theta T_0} \in O(1). \tag{A10}$$

Note that T_0 is uniquely determined by $c_1^* = c_2^* = 1$ if $c_1 = c_2$. The definitions of Eq. (A10) are verified in Sec. VI C. Under these assumptions, we introduce dimensionless variables,

$$\hat{\phi} = \frac{\phi}{\epsilon}, \quad \hat{\psi} = \frac{\psi}{\epsilon}, \quad \hat{t} = \epsilon t^*, \quad \hat{A} = \frac{A}{\epsilon^2},$$

$$\hat{c}_{i \in \{1,2\}} = c_{i \in \{1,2\}}^*. \tag{A11}$$

We then have

$$\dot{\phi} = \frac{\epsilon^2}{T_0}\frac{d\hat{\phi}}{d\hat{t}}, \quad \dot{\psi} = \frac{\epsilon^2}{T_0}\frac{d\hat{\psi}}{d\hat{t}}, \quad \ddot{\phi} = \frac{\epsilon^3}{T_0^2}\frac{d^2\hat{\phi}}{d\hat{t}^2},$$

$$\ddot{\psi} = \frac{\epsilon^3}{T_0^2}\frac{d^2\hat{\psi}}{d\hat{t}^2}. \tag{A12}$$

Using Eqs. (A3), (A6)–(A8), and (A10)–(A12), we rearrange Eq. (A9) to obtain dimensionless motion equations,

$$\epsilon(\hat{\phi} - \hat{\psi}) - 2\epsilon\hat{A}\hat{t}(\epsilon p\hat{\phi} + q)$$

$$+ \epsilon^2 \hat{c}_1 p^2 \frac{d\hat{\phi}}{d\hat{t}} + O(\epsilon^3) = 0,$$

$$-\epsilon(\hat{\phi} - \hat{\psi}) + \epsilon\hat{A}\hat{t}(-\epsilon q\hat{\psi} + p)$$

$$+ \epsilon^2 \hat{c}_2 p^2 \frac{d\hat{\psi}}{d\hat{t}} + O(\epsilon^3) = 0, \tag{A13}$$

where $p = \cos(\pi/8)$ and $q = \sin(\pi/8)$. Ignoring the high-order terms belonging to $O(\epsilon^3)$, it follows from Eq. (A13) that

$$(\phi - \psi) - 2A^* t^* (p\phi + q) + c_1^* p^2 \frac{d\phi}{dt^*} = 0,$$

$$(\phi - \psi) - A^* t^* (-q\psi + p) - c_2^* p^2 \frac{d\psi}{dt^*} = 0. \tag{A14}$$

Converting to the three variables as in Eq. (2), Eq. (A14) becomes Eq. (3), where the angular variables θ_m and θ_s are
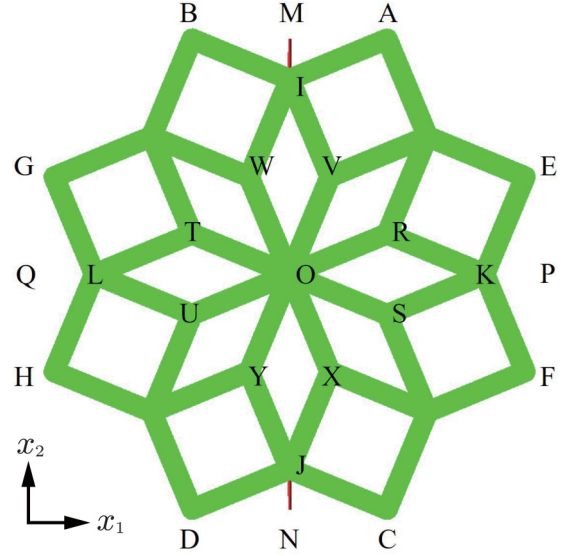

FIG. 11. Front view of the MBD structure with the insertion of two damper units (red elements) in the vertical direction.

represented with the additional variables as

$$\xi = q(\theta_m + \theta_s) - p, \quad \eta = -q(\theta_m - \theta_s) + p$$

$$\Leftrightarrow \theta_m = \frac{\xi - \eta + 2p}{2q}, \quad \theta_s = \frac{\xi + \eta}{2q}. \tag{A15}$$

The initial configuration of the structure has $t = 0$, $\theta_m = 0$, and $\theta_s = 0$, which correspond to $[\xi(0), \eta(0), \zeta(0)] = (-p, p, 0)$.

APPENDIX B: MBD MODELING WITH MEMBER-TO-MEMBER CONTACT

We built the solid-body kinetic system of our proposed structure using MBD software (Adams [28]). The system has 40 beam links of equal length, which are pivotally connected at each end by spherical joints. These links interact via 32 rotational springs and two vertical dampers. Figure 11 shows the front view of the MBD structure in three dimensions. The freestanding structure has multiple degrees of freedom. To realize transformability equivalent to that of the viscoelastic model with two degrees of freedom [Fig. 1(b)], we set the displacement constraints of the nodes as

$$d_1^i = -d_1^j, \quad (i, j) \in \{(E, G), (F, H)\}, \tag{B1}$$

$$d_2^i = -d_2^j, \quad (i, j) \in \{(A, C), (B, D)\}, \tag{B2}$$

$$d_2^i = d_2^j = d_2^k, \quad (i, j, k) \in \{(A, B, M), (C, D, N)\}, \tag{B3}$$

and

$$d_1^I = d_1^J = 0, \quad d_2^K = d_2^L = 0, \tag{B4}$$

where the superscript capitals of d_1 or d_2 correspond to the respective nodes symbolized in Fig. 11; e.g., d_1^A indicates the x_1-axial displacement of node A. The constraint conditions of Eqs. (B1)–(B4) impose on the transformation reflection symmetry about the vertical and horizontal lines through the

center of the structure (node O). The analysis is thus reduced to the first of four structural elements, as shown in Fig. 1(b).

By representing simply the self-contact of the structure, we consider a two-body interaction between nodes R-S, T-U, V-W, and X-Y, which can be described by the Lennard-Jones potential function,

$$V(r_{ij}) = \frac{\alpha}{r_{ij}^{12}} - \frac{\beta}{r_{ij}^{6}}, \qquad (B5)$$

where r_{ij} is the distance between nodes i and j, and $(i, j) \in \{(R, S), (T, U), (V, W), (X, Y)\}$. Provided that V has a min-

imum value in the initial configuration of $r_{ij}(0) = 2\ell q$, the relation $\beta = 2\alpha(2\ell q)^{-6}$ is obtained. Thus, the repulsive forces acting between the two nodes (R-S, T-U, V-W, and X-Y) are expressed by

$$R(r_{ij}) = -\frac{\mathrm{d}V}{\mathrm{d}r_{ij}} = \frac{12\alpha}{r_{ij}^{7}} \left[\frac{1}{r_{ij}^{6}} - \frac{1}{(2\ell q)^{6}} \right]. \qquad (B6)$$

Table I lists the geometric and material parameters of each component in the MBD simulation. As a time-integration technique, we employed Gear's method with a time increment of 0.1 s.

[1] Y. A. Kuznetsov, *Elements of Applied Bifurcation Theory*, 3rd ed. (Springer, New York, 2004).

[2] M. Golubitsky and D. G. Schaeffer, *Singularities and Groups in Bifurcation Theory* (Springer, New York, 1985), Vol. I.

[3] I. Mascolo, Recent developments in the dynamic stability of elastic structures, Front. Appl. Math. Stat. **5**, 51 (2019).

[4] S. P. Timoshenko and J. M. Gere, *Theory of Elastic Stability*, 2nd ed. (Dover, New York, 2009).

[5] J. M. T. Thompson and G. W. Hunt, *A General Theory of Elastic Stability* (Wiley, New York, 1973).

[6] H. Yabuno, Buckling of a beam subjected to electromagnetic force and its stabilization by controlling the perturbation of the bifurcation, Nonlinear Dyn. **10**, 271 (1996).

[7] H. Yabuno, Y. Kurata, and N. Aoshima, Effect of Coulomb damping on buckling of a two-rod system, Nonlinear Dyn. **15**, 207 (1998).

[8] S. S. Antman, *Nonlinear Problems of Elasticity*, 2nd ed. (Springer, New York, 2005).

[9] A. H. Alhadidi and J. M. Gibert, A new perspective on static bifurcations in the presence of viscoelasticity, Nonlinear Dyn. **103**, 1345 (2021).

[10] T. G. Sano and H. Wada, Snap-buckling in asymmetrically constrained elastic strips, Phys. Rev. E **97**, 013002 (2018).

[11] L. J. Gibson and M. F. Ashby, *Cellular Solids: Structure and Properties*, 2nd ed. (Cambridge University Press, Cambridge, 1997).

[12] N. Triantafyllidis and M. W. Schraad, Onset of failure in aluminum honeycombs under general in-plane loading, J. Mech. Phys. Solids **46**, 1089 (1998).

[13] S. D. Papka and S. Kyriakides, Biaxial crushing of honeycombs. Part I: Experiments, Intl. J. Solids Struct. **36**, 4367 (1999).

[14] S. D. Papka and S. Kyriakides, In-plane biaxial crushing of honeycombs. Part II: Analysis, Intl. J. Solids Struct. **36**, 4397 (1999).

[15] N. Ohno, D. Okumura, and H. Noguchi, Microscopic symmetric bifurcation condition of cellular solids based on a homogenization theory of finite deformation, J. Mech. Phys. Solids **50**, 1125 (2002).

[16] H. Tanaka and Y. Shibutani, Large deformability of 2D framed structures connected by flexible joints, J. Solid Mech. Mater. Eng. **2**, 1037 (2008).

[17] C. Combescure, P. Henry, and R. S. Elliott, Post-bifurcation and stability of a finitely strained hexagonal honeycomb subjected to equi-biaxial in-plane loading, Intl. J. Solids Struct. **88-89**, 296 (2016).

[18] T. Mullin, S. Deschanel, K. Bertoldi, and M. C. Boyce, Pattern Transformation Triggered by Deformation, Phys. Rev. Lett. **99**, 084301 (2007).

[19] H. Tanaka and Y. Shibutani, In-plane mechanical behaviors of 2D repetitive frameworks with four-coordinate flexible joints and elbowed beam members, J. Mech. Phys. Solids **57**, 1485 (2009).

[20] Y. Chen, T. Li, F. Scarpa, and L. Wang, Lattice Metamaterials with Mechanically Tunable Poisson's Ratio for Vibration Control, Phys. Rev. Appl. **7**, 024012 (2017).

[21] K. Gopalsamy and P.-X. Weng, Feedback regulation of logistic growth, Intl. J. Math. Math. Sci. **16**, 177 (1993).

[22] Y. Lv, L. Chen, and F. Chen, Stability and bifurcation in a single species logistic model with additive Allee effect and feedback control, Adv. Differ. Equ. **2020**, 129 (2020).

[23] H. Tanaka, Y. Shibutani, S. Izumi, and S. Sakai, Planar mobility modes of 8-bar-jointed structures with a single degree of freedom, Intl. J. Solids Struct. **49**, 1712 (2012).

[24] H. Tanaka, Bi-stiffness property of motion structures transformed into square cells, Proc. R. Soc. A **469**, 20130063 (2013).

[25] H. Tanaka, T. Nakanishi, and Y. Shibutani, Switching between two types of auxetic behavior of two-dimensional periodic cells with square rotation, Phys. Status Solidi B **253**, 718 (2016).

[26] H. Tanaka, K. Hamada, and Y. Shibutani, Transition mechanism for a periodic bar-and-joint framework with limited degrees of freedom controlled by uniaxial load and internal stiffness, R. Soc. Open Sci. **5**, 180139 (2018).

[27] MATLAB, version 9.9.0.1592791 (R2020b) (The MathWorks, Inc., Natick, MA, 2020), https://www.mathworks.com/help/matlab/ref/ode45.html (access date: October 8, 2021).

[28] Adams, version 2018.0.0-CL562971 (MSC software Corp., Irvine, CA, 2018), https://www.mscsoftware.com/product/adams (access date: October 8, 2021).

[29] See Supplemental Material at http://link.aps.org/supplemental/10.1103/PhysRevE.104.045001 for animations of the critical transformations of the self-contacted structure.

[30] https://jp.edanz.com/ac